ChemPubSoc Europe

DOI: 10.1002/cphc.201300713

Global Reaction Pathways in the Photodissociation of I_3^- Ions in Solution at 267 and 400 nm Studied by Picosecond X-ray Liquidography

Kyung Hwan Kim,[a, b] Hosung Ki,[a, b] Key Young Oang,[a, b] Shunsuke Nozawa,[c] Tokushi Sato,[c] Joonghan Kim,[d] Tae Kyu Kim,[e] Jeongho Kim,[f] Shin-ichi Adachi,[c] and Hyotcherl Ihee*[a, b]

The mechanism of a photochemical reaction involves the formation and dissociation of various short-lived species on ultrafast timescales and therefore its characterization requires detailed structural information on the transient species. By making use of a structurally sensitive X-ray probe, time-resolved X-ray liquidography (TRXL) can directly elucidate the structures of reacting molecules in the solution phase and thus determine the comprehensive reaction mechanism with high accuracy. In this work, by performing TRXL measurements at two different wavelengths (400 and 267 nm), the reaction mechanism of I_3^- photolysis, which changes subtly depending on the excitation wavelength, is elucidated. Upon 400 nm photoexcitation, the I_3^- ion dissociates into I_2^- and I. By contrast, upon 267 nm photoexcitation, the I_3^- ion undergoes both two-body dissociation ($I_2^- + I$) and three-body dissociation ($I^- + 2I$) with 7:3 molar ratio. At both excitation wavelengths, all the transient species ultimately disappear in 80 ns by recombining to form the I_3^- ion nongeminately. In addition to the reaction dynamics of solute species, the results reveal the transient structure of the solute/solvent cage and the changes in solvent density and temperature as a function of time.

1. Introduction

Photochemical reactions often occur on ultrafast timescales and involve the formation and dissociation of various short-lived chemical species. To elucidate the mechanism of such reactions, detailed structural information on the transient species is required. For that purpose, various time-resolved optical spectroscopic techniques have been used to capture the dynamics of rapidly reacting molecules with high sensitivity and temporal resolution.[1–6] However, in the typical time-resolved spectroscopic techniques, the observables are related to optical resonances of the molecules and cannot be correlated directly with the changes in atomic arrangement of the molecules. As an alternative, replacement of the optical probe by structural probes, such as X-ray absorption[7–10] or X-ray diffraction,[11–22] allows us to directly obtain the detailed structural information including the structure of short-lived solute species and solvent rearrangement around the solutes. Based on this idea, time-resolved X-ray liquidography (TRXL) or so-called time-resolved X-ray solution scattering has been applied to various solution-phase molecular systems ranging from small molecules[11–19] and proteins[20–22] to nanoparticles[23–25] and protein–nanoparticle complexes,[26] thereby revealing the reaction pathways and intermediates of the reactions.

Photodissociation of the I_3^- ion in solution was studied by using various time-resolved spectroscopic techniques.[27–37] One of the main interests in those studies was the reaction mechanism that varies with the excitation wavelength. Upon UV excitation, in principle the I_3^- ion has three candidate dissociation channels: two-body dissociation ($I_2^- + I$), three-body dissociation ($I^- + I + I$), and I_2 formation ($I_2 + I^-$) as depicted in Figure 1. Ruhman and co-workers identified two-body dissociation of I_3^- in ethanol upon photoexcitation at 308 nm by detecting the coherent oscillation of the transient absorption signal that arises from coherently excited vibrational motion of the I_2^- fragment.[27,28,38] They also measured faster processes, such as vibrational dephasing and geminate recombination of the I_2^- fragment, which occur on the timescales of 400 fs and 4 ps, respectively. Later, Vohringer and co-workers studied photodisso-

[a] Dr. K. H. Kim, H. Ki, K. Y. Oang, Prof. H. Ihee
Center for Nanomaterials and Chemical Reactions
Institute for Basic Science, Daejeon 305-701 (Republic of Korea)
Fax: (+82) 42-350-2810
E-mail: hyotcherl.ihee@kaist.ac.kr

[b] Dr. K. H. Kim, H. Ki, K. Y. Oang, Prof. H. Ihee
Department of Chemistry, KAIST
Daejeon 305-701 (Republic of Korea)

[c] Prof. S. Nozawa, Dr. T. Sato, Prof. S.-i. Adachi
Institute of Materials Structure Science
High Energy Accelerator Research Organization (KEK)
1-1 Oho, Tsukuba, Ibaraki 305-0801 (Japan)

[d] Prof. J. Kim
Department of Chemistry, The Catholic University of Korea
Bucheon 420-743 (Republic of Korea)

[e] Prof. T. K. Kim
Department of Chemistry and Chemistry Institute of Functional Materials
Pusan National University, Busan 609-735 (Republic of Korea)

[f] Prof. J. Kim
Department of Chemistry, Inha University
Incheon 402-751 (Republic of Korea)

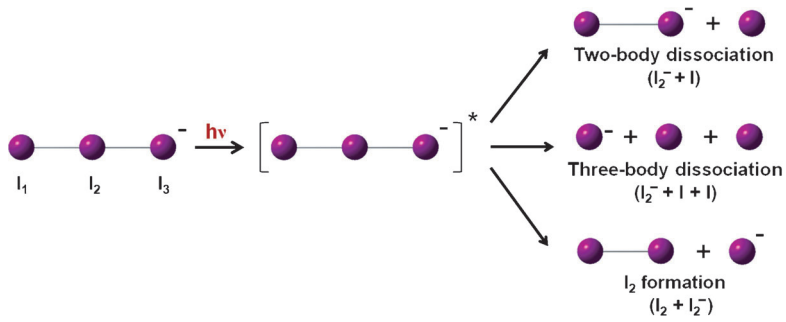

Figure 1. Schematic of candidate reaction pathways for photodissociation of the I_3^- ion in solution: two-body dissociation ($I_2^- + I$), three-body dissociation ($I^- + 2I$), and another two-body dissociation leading to I_2 formation ($I_2 + I^-$).

ciation of the I_3^- ion using transient absorption at two different excitation wavelengths, 266 and 400 nm, and determined the transient population distribution of vibrational states and the quantum yield of the I_2^- fragment formation (that is, two-body dissociation).[29] From that study, it was found that the quantum yield of two-body dissociation is almost unity with 400 nm excitation but decreases to 0.8 with 266 nm excitation. This reduced quantum yield was attributed to the increasing contribution of the three-body dissociation ($I^- + I + I$) pathway. However, evidence of three-body dissociation was not directly observed in the transient absorption measurement because transient absorption at the probe wavelength was sensitive to the I_2^- fragment, but not to the photoproducts of three-body dissociation (I and I^-). In contrast, because X-rays scatter off all the atoms in a molecule, TRXL can detect any intermediates and products of the reaction. Furthermore, it is also sensitive to solute–solvent interaction (cage term) induced by the formation of transient solute species. Thus, TRXL is well suited for studying the entire pathways of a reaction.[11–22,39–43] In this work, we investigated the change of reaction mechanism of I_3^- photodissociation depending on the excitation wavelength by directly measuring the structures of transient solute species, the cage environment, and the solvent hydrodynamics by using TRXL.

TRXL can determine the bond lengths with sub-angstrom accuracy, which is crucial for keeping track of the structural changes of reacting molecules. For I_3^- photodissociation, we need to characterize I–I distances of five I–I pairs: I_1–I_2, I_2–I_3, and I_1–I_3 of the parent I_3^- molecule, I–I of I_2, and I–I of the I_2^- fragment. Especially, the I–I distances of I_2 and I_2^- are very different from each other, as shown in Figure 2, and can be used as criteria for distinguishing between three different reaction pathways. By taking advantage of the superb structural sensitivity of TRXL, we are able to determine the branching ratio of various reaction pathways depending on the excitation wavelength.

As shown in Figure 3a, the I_3^- ion can be photoexcited at a wavelength of either 267 or 400 nm. We performed high-

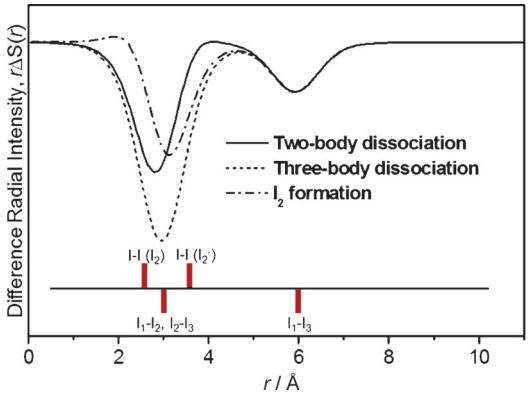

Figure 2. Theoretical difference radial distribution functions (RDFs) corresponding to three different reaction channels. The difference RDFs were constructed by a combination of I–I distances for five I–I pairs: I_1–I_2, I_2–I_3, and I_1–I_3 of the parent I_3^- molecule, I–I of I_2, and I–I of I_2^-. The distance of each I–I pair is indicated as a line at the bottom. For the sake of clarity, here only the contribution from the solute molecules is considered. The lines above the baseline correspond to the positive contributions reflecting the formation of bonds, whereas the lines below the baseline correspond to the negative contributions reflecting the depletion of bonds.

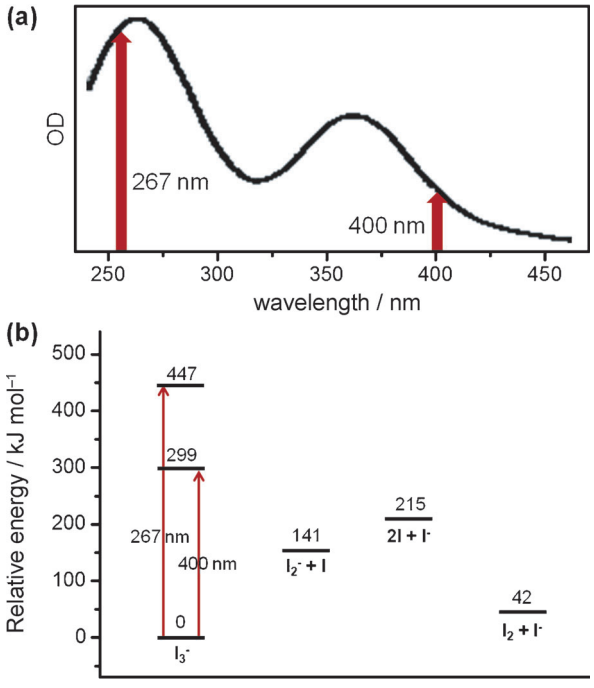

Figure 3. a) Absorption spectrum of the I_3^- ion in methanol solution. Two different excitation wavelengths (400 and 267 nm) are indicated by vertical arrows. b) Energies of the reaction pathways involved in the photodissociation of the I_3^- ion obtained from DFT calculations. The energy of each pathway was calculated by a combination of the energies of solute species involved in the pathway. For convenience, the relative energy of the parent I_3^- ion was set to zero. Although excitations at 400 and 267 nm both provide enough energy for each reaction pathway to occur, the amount of excess energy varies depending on the excitation wavelength and may change the branching ratio between different reaction pathways.

level density functional theory (DFT) calculations (details are provided in the Experimental Section) to obtain the energies for various reaction pathways involved in the photodissociation of the I_3^- ion, as shown in Figure 3b. Although excitations at 400 and 267 nm both provide enough energy for all reaction pathways, the amount of excess energy varies depending on the excitation wavelength and may change the branching ratio between different reaction channels. In this work, we investigated the detailed reaction mechanism of photodissociation of the I_3^- ion in methanol by using TRXL measurements. By comparing the reaction pathways on excitation at two different wavelengths (400 and 267 nm), we elucidate the wavelength dependence of the reaction mechanism.

2. Results and Discussion

The scheme of TRXL experiments performed in this study is shown in Figure 4. Scattering patterns, $S(q,t)$, from I_3^- solution were measured at various positive time delays after laser excitation (that is, the X-ray pulse arrives after the laser pulse). The reference scattering pattern was also measured at a negative time delay (that is, the X-ray pulse arrives before the laser pulse) and was subtracted from the ones measured at positive time delays to obtain the time-dependent difference scattering patterns, $\Delta S(q,t)$, which contain information on the structural change of the reacting molecules only. For simple analysis and improved signal-to-noise ratio, the difference scattering pattern was integrated along the azimuthal direction to obtain the difference scattering pattern. The details of the experimental procedure and analysis are described in the Experimental Section. To study the wavelength dependence of the photodissociation pathways, two different excitation wavelengths (400 and 267 nm) were used. To cover the entire time range of a complete reaction including photodissociation, temperature change, volume expansion, and nongeminate recombination, we measured the difference scattering patterns at various time delays spanning from 100 ps to 3 μs. Difference scattering curves at 100 ps time delay with 400 and 267 nm excitations are compared in Figure 4. The two scattering patterns are clearly different, which indicates that the reaction pathways change depending on the excitation wavelength.

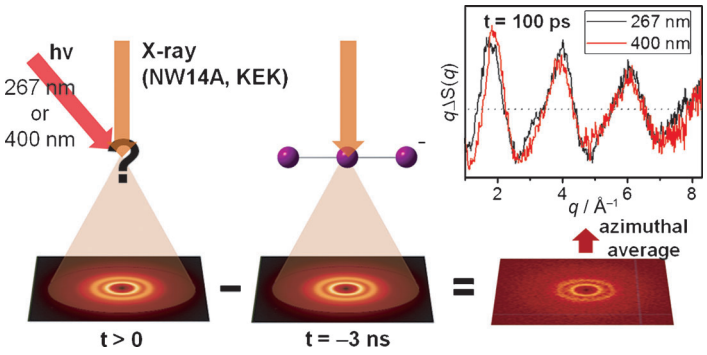

Figure 4. Schematic of the TRXL experiment. Scattering patterns from I_3^- solution are measured before and after laser excitation and these patterns are subtracted from each other to extract information on the structural change of the reacting molecules only. To study wavelength-dependent pathways in the photodissociation, two different excitation wavelengths (400 and 267 nm) were used. The one-dimensional scattering curve is obtained by azimuthal averaging. Data are measured at well-defined time delays spanning from 100 ps to 3 μs. Difference scattering patterns at 100 ps with 267 and 400 nm excitation are compared and show slightly different features, thus indicating that the reaction pathways change depending on the excitation wavelength.

Structural Parameters of Chemical Species Involved in the Reaction

The structural parameters of the parent I_3^- ion and transient I_2^- ion were determined in our previous work, as summarized in Table 1.[44] The details of the structural analysis of I_3^- and I_2^- ions are also described in our previous work. Briefly, to extract the structures of I_3^- and I_2^- ions from the difference scattering pattern at 100 ps time delay obtained from the TRXL measurements, least-squares fitting was employed with four variable structural parameters. The variables are three I–I distances for the I_3^- ion (R_1, R_2, and R_3 for the distances between I_1 and I_2, I_2 and I_3, I_1 and I_3, respectively) and the I–I distance for the I_2^- fragment (R_4). The theoretical scattering pattern was calculated by standard diffuse X-ray scattering formulas with these parameters as variables. The chi-squared (χ^2) estimator was used to calculate the deviation between the experimental and theoretical scattering patterns. By minimizing the χ^2 value, we were able to find the optimal structures of I_3^- and I_2^- ions. From the analysis, R_1, R_2, R_3, and R_4 were determined to be 2.94, 3.03, 5.97, and 3.59 Å, respectively, with sub-angstrom accuracy.[44] The I–I bond length of I_2 was determined to be 2.66 Å by high-level DFT calculation, the details of which are described in Experimental Section. This value for the I–I bond length is close to the value (2.67 Å) determined from a TRXL experiment on I_2 in CCl_4.[45] We used these values of structural parameters for the analysis presented herein.

Table 1. Structural parameters of the chemical species used in the data analysis.

Structural parameter	I_3^-			I_2^-	I_2
	I_1–I_2	I_2–I_3	I_1–I_3		
Distance [Å]	2.94[a]	3.03[a]	5.97[a]	3.59[a]	2.66[b]

[a] Values determined by a previous TRXL study.[44] [b] Value determined by DFT calculation.

Photodissociation of I_3^- with 400 nm Excitation

Experimental difference scattering curves, $q\Delta S(q,t)$, measured with 400 nm laser excitation at time delays from 100 ps to 3 μs are shown in Figure 5a. As described above, the experimental difference scattering curves were obtained by subtracting the scattering signal measured at a negative time delay (−3 ns) from the scattering signal measured at positive time delays. With the differencing scheme, only the contributions from reacting molecules are em-

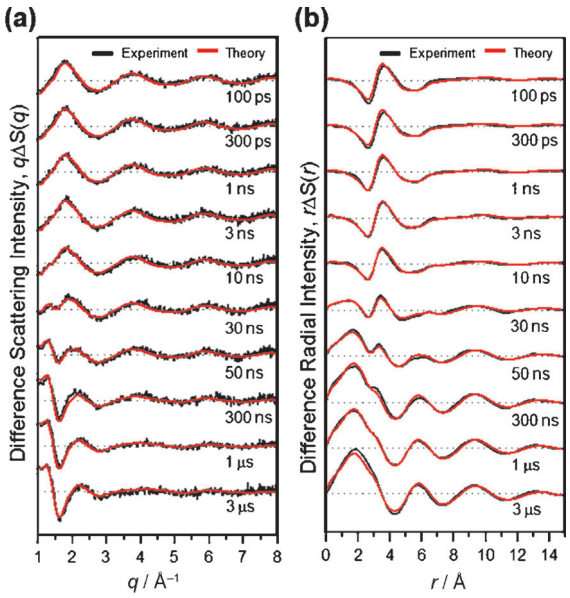

Figure 5. Time-resolved difference X-ray scattering curves of the I_3^- ion in methanol measured with 400 nm laser excitation. a) Experimental difference scattering curves, $q\Delta S(q,t)$, at various time delays (black) and their theoretical fits (red) are shown together. b) Corresponding difference RDFs, $r\Delta S(r,t)$, obtained by sine-Fourier transformation of $q\Delta S(q,t)$ in (a).

phasized with all other contributions from nonreacting molecules removed. The difference scattering intensities show oscillatory features along the q axis. Such oscillations are the signatures of 1) structural change of reacting solute molecules, 2) change of solute–solvent interaction (cage), and 3) solvent responses. The shape and amplitude of the oscillatory features vary with the time delay, thus reflecting the reaction dynamics. The amplitude of the difference scattering curve does not increase at early time delays, which indicates that the photodissociation occurs impulsively within our time resolution (100 ps). The oscillatory features at high q values become smaller in approximately 80 ns due to the recovery of the parent I_3^- ion by nongeminate recombination with the bimolecular rate constant of $2.17(\pm1.44)\times10^{10}\,M^{-1}s^{-1}$. The experimental scattering curves were fitted by the maximum likelihood estimation (MLE) using the χ^2 estimator. Theoretical difference scattering curves are the best fits of the experimental scattering curves and are shown in Figure 5a together with the experimental curves.

The difference scattering intensities in q-space, $q\Delta S(q,t)$, can be converted to difference radial intensities in real space, $r\Delta S(r,t)$, by sine-Fourier transformation. The resultant difference radial distribution functions (RDFs) shown in Figure 5b represent the change of interatomic distances (r) in the molecules participating in the reaction and thus provide a more intuitive picture of the structural change of the molecules. For example, positive and negative features in the difference RDFs indicate the formation and elimination of an atomic pair at a certain distance, respectively. Therefore, by analyzing the RDFs, we can directly identify the chemical species involved in the reaction and quantify the population of each species at an instant during the progress of the reaction.

From previous time-resolved spectroscopic studies on photodissociation of the I_3^- ion in the solution phase,[27–30,38] it was found that two-body dissociation ($I_2^- + I$) is the major reaction pathway. Also, it was proposed that the contribution of two-body dissociation decreases with 266 nm excitation, probably due to an increasing contribution of three-body dissociation ($I^- + I + I$). To confirm the results of the previous studies and elucidate the detailed mechanism of I_3^- photodissociation depending on the excitation wavelength, we analyzed our TRXL data by considering all the possible candidate reaction pathways: two-body dissociation ($I_2^- + I$), three-body dissociation ($I^- + I + I$), and two-body dissociation leading to I_2 formation ($I_2 + I^-$). As X-rays scatter from every atom in the molecules, the TRXL measurement should be equally sensitive to the three reaction pathways. Details of the fitting and error analysis are given in the Experimental Section and in our previous work.[13,14,18]

The results of fitting analysis for the TRXL data obtained with 400 nm excitation are shown in Figure 6. The difference scattering curve at 100 ps is presented as an example because

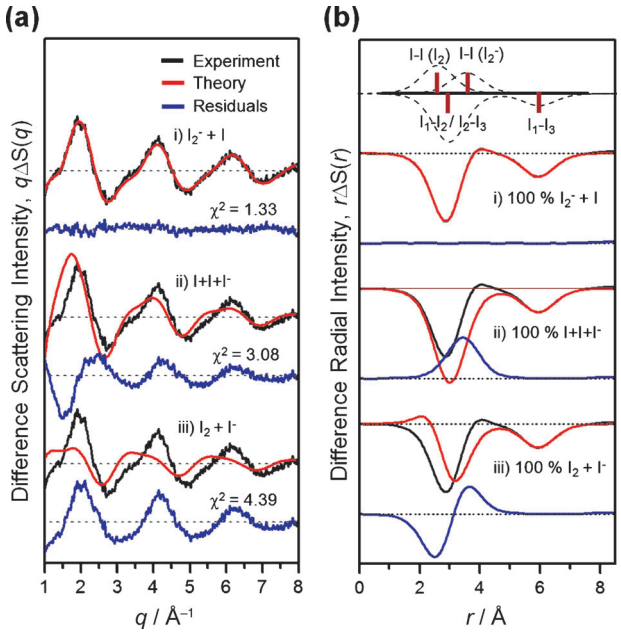

Figure 6. Determination of the reaction pathway of I_3^- photodissociation in methanol with 400 nm laser excitation in a) q-space and b) r-space. a) The theoretical difference scattering curve (red) for each candidate pathway is shown together with the experimental difference scattering curve at 100 ps (black). The model employing only the two-body dissociation pathway gives a much better fit than the models employing the three-body dissociation and I_2 formation pathways, thus indicating that two-body dissociation is the dominant reaction pathway with 400 nm laser excitation. The model employing all three reaction pathways gives the same quality of fit as the two-body dissociation model with the contributions from the three-body dissociation and I_2 formation pathways converging to zero. b) RDFs, $r\Delta S(r,t)$, of the solute-only term. Bond lengths and their contributions to various I–I pairs are indicated as red bars and dashed curves, respectively, at the top. The red bars above the baseline correspond to the positive contributions reflecting the formation of reaction intermediates and products, whereas the red bars below the baseline correspond to the negative contributions reflecting the depletion of the reactant (I_3^- ion). With the model employing only two-body dissociation, the experimental and theoretical RDFs of the solute-only term are in good agreement.

dissociated fragments are dominant at early time delays. It is clearly seen in Figure 6a that the theoretical scattering curve built from the two-body dissociation pathway fits the experimental scattering curve much better than the ones built from three-body dissociation or I_2 formation, with χ^2 values of 1.33, 3.08, and 4.39 for two-body dissociation, three-body dissociation, and I_2 formation, respectively. To consider the possibility that the three pathways occur simultaneously, we also tested a fit with a linear combination of the three reaction pathways. From the optimization of the branching ratio of the three pathways, we found that the contributions from three-body dissociation and I_2 formation converge to zero within the error range. Thus, we confirmed that two-body dissociation is the only reaction pathway of I_3^- photodissociation with 400 nm excitation.

By comparing the experimental and theoretical RDFs, $r\Delta S(r,t)$, in real space as shown in Figure 6b, we can obtain a more intuitive picture of the structural change involved in each reaction pathway. The solute-only term was carefully extracted from the difference scattering curve at 100 ps to emphasize only the contribution from various I–I pairs of solute molecules. The decomposition of the difference scattering curves into solute, cage, and solvent terms is described in Figure 10 and its related text. Bond lengths of various I–I pairs are indicated as lines at the top of Figure 6b and can be used as a guideline for identifying the detailed structural change of reacting molecules. The lines above the baseline correspond to the positive contributions reflecting the formation of reaction intermediates and products, whereas the lines below the baseline correspond to the negative contributions reflecting the depletion of the reactant (I_3^- ion). For the model employing only the two-body dissociation ($I_2^- + I$) pathway, the experimental and theoretical RDFs match very well. For the model employing only the three-body dissociation ($I + I + I^-$) pathway, the residual (= experimental RDF − theoretical RDF; blue line) is positive at approximately 3.6 Å, which corresponds to the I–I distance of the I_2^- ion. This observation means that more I_2^- ions are formed in the experiment than in the three-body dissociation model. For the model employing only the I_2 formation ($I_2 + I^-$) pathway, the residual is positive at approximately 3.6 Å, which is the I–I distance of the I_2^- ion, and negative at approximately 2.7 Å, which corresponds to the I–I distance of I_2. This observation means that 1) more I_2^- ions and 2) fewer I_2 molecules are formed in the experiment than in the I_2 formation model. Thus, the nonzero residuals in both models support the notion that only two-body dissociation occurs with 400 nm excitation.

From the analysis of the data over the entire time range from 100 ps to 3 μs, we also obtained the reaction dynamics associated with the concentration changes of chemical species involved in the reaction. Figure 9a shows time-dependent concentration changes of transient solute species after 400 nm laser excitation. After photoexcitation, 32 ± 5% of excited I_3^- ions dissociate into I_2^- and I through two-body dissociation in less than 100 ps, which is the time resolution of our experiment. The parent I_3^- ion is regenerated by nongeminate recombination of I_2^- and I in approximately 80 ns with the bimolecular rate constant of $2.17(\pm 1.44) \times 10^{10}\ M^{-1}s^{-1}$. The timescale of each step is summarized in Figure 12a. Besides the concentration dynamics, we also obtained information on the temperature change and volume expansion of solvent. The nonreacting portion (68 ± 5%) of excited I_3^- ions dissipate the heat to the environment and the temperature of the excited volume increases by 0.41 K at early time delays. After about 10 ns, volume expansion occurs and the solvent density decreases by $0.42\ kg\,m^{-3}$ at late time delays.

Photodissociation of I_3^- with 267 nm Excitation

Experimental difference scattering curves, $q\Delta S(q)$, measured with 267 nm laser excitation at time delays from 100 ps to 3 μs are shown in Figure 7a. The TRXL data with 267 nm excitation were acquired and analyzed in the same manner as the 400 nm excitation data. As for the 400 nm data, the difference scattering intensities exhibit oscillatory features that vary with time delay. However, as shown in the inset of Figure 4, the 267 nm data have different oscillatory features from the 400 nm data, which suggests that the reaction mechanism changes with the excitation wavelength. Theoretical difference scattering curves, which are the best fits of the experimental scattering curves, are displayed together with the experimental curves in Figure 7a. The difference scattering curves in q-space were sine-Fourier transformed to difference RDFs in real space, which are shown in Figure 7b.

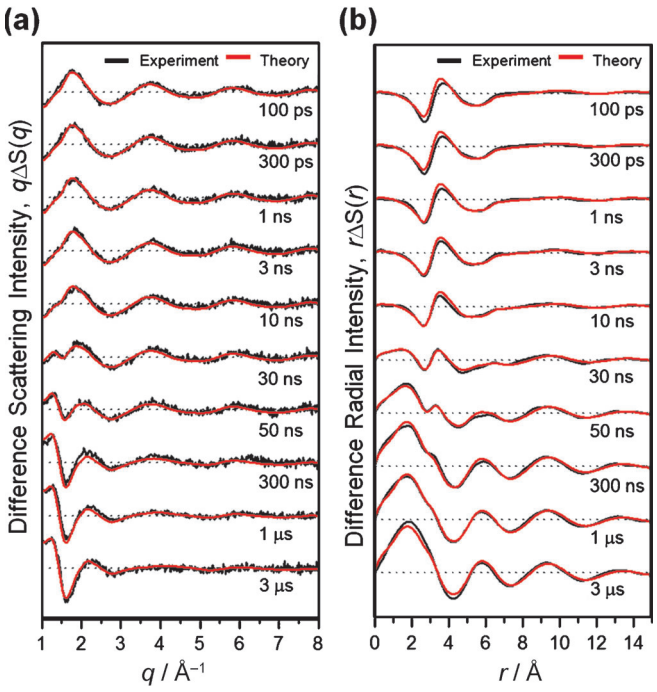

Figure 7. Time-resolved difference X-ray scattering curves of the I_3^- ion in methanol measured with 267 nm laser excitation. a) Experimental difference scattering curves, $q\Delta S(q,t)$, at various time delays (black) and their theoretical fits (red) are shown together. b) Corresponding difference radial difference functions, $r\Delta S(r,t)$, obtained by sine-Fourier transformation of $q\Delta S(q,t)$ in (a).

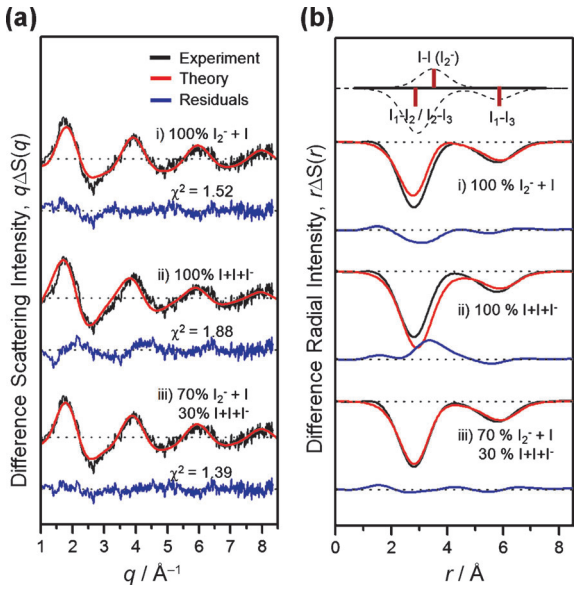

Figure 8. Determination of the reaction pathway of I_3^- photodissociation in methanol with 267 nm laser excitation in a) *q*-space and b) *r*-space. a) The theoretical difference scattering curve (red) for each candidate pathway is shown together with the experimental difference scattering curve at 100 ps (black). The models employing the two-body and three-body dissociation pathways give similarly good fitting qualities, thereby indicating the possibility of multiple reaction pathways. The best fit was obtained with a model employing all three reaction pathways. The optimum ratio of the contributions of two-body and three-body dissociation was determined to be 7:3, whereas the I_2 formation pathway does not contribute at all. b) RDFs, $r\Delta S(r,t)$, of the solute-only term. Bond lengths and their contributions to various I–I pairs are indicated as red bars and dashed curves, respectively, at the top. The red bars above the baseline correspond to the positive contributions reflecting the formation of reaction intermediates and products, whereas the red bars below the baseline correspond to the negative contributions reflecting the depletion of the reactant (I_3^- ion). With the model employing the two-body and three-body dissociation pathways at a branching ratio of 7:3, the experimental and theoretical RDFs of the solute-only terms are in good agreement.

As for the 400 nm data, we performed the global fit analysis of the 267 nm data by considering three candidate reaction pathways. The results of the analysis are shown in Figure 8. We present the difference scattering curve at 100 ps, since dissociated fragments are dominant at early time delays. It can be seen that the model employing the two-body dissociation pathway still fits the experimental curve better than three-body dissociation or I_2 formation, with χ^2 values of 1.52, 1.88, and 4.02 for two-body dissociation, three-body dissociation, and I_2 formation, respectively. However, unlike the case of 400 nm excitation, the difference in the fit quality between the two-body and three-body dissociation models is not large, and the fit quality of the two-body dissociation model is worse than for the 400 nm data. This observation suggests that the reaction might proceed through multiple reaction pathways. To consider the possibility that the three pathways occur simultaneously, we tried to fit with a linear combination of all three reaction pathways. By optimizing the branching ratio of the three pathways, we obtained the best fit ($\chi^2 = 1.39$) when the two-body and three-body pathways occur with a branching ratio of 7:3, which is in contrast to the reaction mechanism with 400 nm excitation. The results of the analysis for the 400 and 267 nm excitations are compared in more detail in the next section.

To have a more intuitive picture of the structural change involved in the reaction, the experimental and theoretical RDFs, $r\Delta S(r,t)$, in real space are compared in Figure 8b. The solute-only term was carefully extracted from the difference scattering curve at 100 ps to emphasize the contribution from various I–I pairs of solute molecules. Bond lengths of various I–I pairs are indicated as lines at the top of Figure 8b and can be used as a guideline for identifying the detailed structural change of reacting molecules. For the model employing only the two-body dissociation ($I_2^- + I$) pathway, the quality of the fit is not as perfect as that for the 400 nm case, and the residual (= experimental RDF − theoretical RDF; blue line) is slightly negative at approximately 3.4 Å, which is close to the I–I distance of the I_2^- ion. This observation means that fewer I_2^- ions are formed in the experiment than in the two-body dissociation model. For the model employing only the three-body dissociation ($I + I + I^-$) pathway, the residual is slightly positive at approximately 3.6 Å, which corresponds to the I–I distance of the I_2^- ion. This observation means that more I_2^- ions are formed in the experiment than in the three-body dissociation model. Combining these two observations, we can infer that two-body dissociation occurs less and three-body dissociation occurs more with 267 nm excitation than with 400 nm excitation, which agrees with the result of the fitting analysis described above. If the two-body and three-body dissociation pathways occur with 7:3 branching ratio, we can see that the experimental and theoretical RDFs of the solute-only terms are in good agreement, giving a negligible residual. Therefore, we conclude that the two-body and three-body dissociation pathways occur competitively with 267 nm excitation. The real-space RDFs obtained from the best fits of the experimental difference scattering curves are compared for 400 and 267 nm excitations in the next section.

We also obtained the reaction dynamics related to the concentration changes of chemical species involved in the reaction. Figure 9b shows the time-dependent concentration changes of transient solute species after 267 nm laser excitation. After photoexcitation, 28 ± 3% of excited I_3^- ions dissociate into 1) $I_2^- + I$ through two-body dissociation and 2) $2I + I^-$ through three-body dissociation in less than 100 ps. During the reaction, the I_2^- ion is formed by nongeminate recombination of I^- and I in about 60 ns with the bimolecular rate constant of $4.61(\pm 1.97) \times 10^{10}\,M^{-1}s^{-1}$ and the parent I_3^- ion is regenerated by nongeminate recombination of I_2^- and I in approximately 80 ns with the bimolecular rate constant of $2.70(\pm 0.78) \times 10^{10}\,M^{-1}s^{-1}$. The timescale of each reaction step is summarized in Figure 12b. Besides the concentration dynamics, we also obtained information on the temperature change and volume expansion of the solvent. The nonreacting portion (72 ± 3%) of excited I_3^- ions generate heat to the environment, which increases the temperature of the excited volume by 0.45 K at early time delays. After about 10 ns, the excited volume expands and the solvent density decreases by 0.47 kg m^{-3} at late time delays. The changes in both tempera-

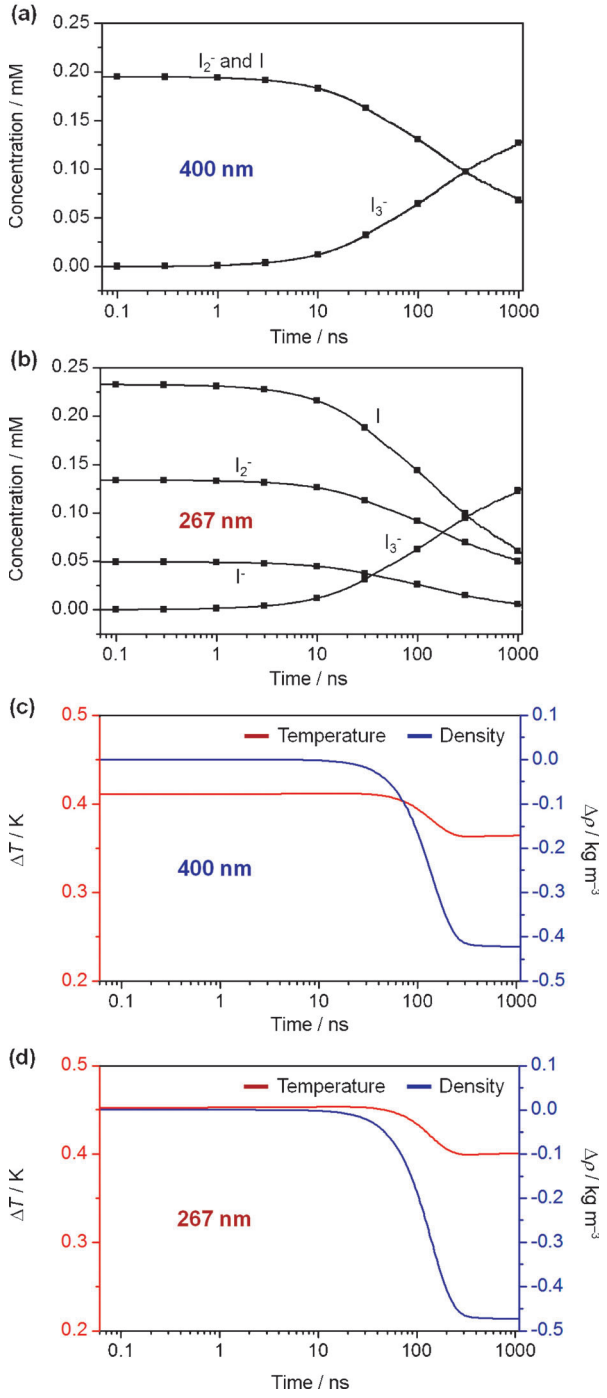

Figure 9. a) Time-dependent concentration changes of various transient solute species after photodissociation of the I_3^- ion in methanol with 400 nm excitation. The name of each species is indicated above each trace. The squares indicate the time points at which we obtained the scattering data. b) Time-dependent concentration changes of various transient solute species after photodissociation of the I_3^- ion in methanol with 267 nm excitation. c) Time-dependent changes of solvent temperature (red) and density (blue) after photodissociation of the I_3^- ion in methanol with 400 nm excitation. d) Time-dependent changes of solvent hydrodynamics after photodissociation of the I_3^- ion with 267 nm excitation.

ture and density are larger with 267 nm excitation than with 400 nm excitation, probably due to a higher absorption coefficient at 267 nm and larger nonreacting portion, thus leading to more excess energy dissipated as heat.

Excitation Wavelength-Dependent Structural Dynamics

From the fitting analysis of the TRXL data, we revealed that the reaction mechanism of I_3^- photodissociation changes with the excitation wavelength. With 400 nm excitation, the reaction occurs through only two-body dissociation. In contrast, with 267 nm excitation, the reaction proceeds through both two-body and three-body dissociation with the branching ratio of 7:3. The reaction mechanism of I_3^- photodissociation dependent on excitation wavelength is summarized in Figure 12. These findings confirm that two-body and three-body dissociation pathways occur competitively on excitation at 267 nm as suggested by a previous study.[29,32] In particular, we determined the branching ratio of two-body and three-body dissociation (7:3) based on the direct structural evidence obtained from TRXL data.

The TRXL measurement is sensitive not only to structural changes of solute molecules, but also to solute–solvent interaction (cage term) and solvent hydrodynamics. To distinguish these different components constituting the TRXL signal, we decomposed the difference RDF, $r\Delta S(r)$, at each time delay into three components: the solute-only term, the cage term, and the solvent-only term. In Figure 10, the decomposed RDFs for 400 nm excitation (black) and 267 nm excitation (red) are shown together. At the bottom of each plot, the distances of major atom–atom pairs are indicated as lines. The lines above the baseline correspond to the positive contributions reflecting the formation of reaction intermediates and products as well as the change in their associated solvent environment, whereas the lines below the baseline correspond to the negative contributions reflecting the depletion of the reactant (I_3^- ion) and the change in its related solvent environment. As the reaction progresses, the overall amplitudes of the oscillatory features in the difference RDFs decrease due to geminate recombination.

The solute-only RDFs extracted from the 100 ps scattering curves with 400 and 267 nm excitations are compared in Figure 11 a. The solute-only term at 100 ps was already used to determine the reaction pathway in Figure 6 and Figure 8. The negative peak near 6 Å indicates the depletion of the I_1–I_3 distance in the parent I_3^- ion and is identical in both RDFs. In contrast, the broad feature at 3–4 Å is different in the two RDFs. This feature arises from a combination of 1) depletion of the I–I bond (I_1–I_2 or I_2–I_3) in the parent I_3^- ion (negative peak at $\approx$3 Å) and 2) formation of the I–I bond in the I_2^- ion (positive peak at $\approx$3.6 Å). The former contribution is common to both two-body and three-body dissociation pathways, whereas the latter is characteristic of two-body dissociation. As the contribution of two-body dissociation decreases with 267 nm excitation, the broad feature at 3–4 Å becomes less positive accordingly.

The solute–solvent cage term, which arises from the change of interatomic distances for I–$O_{solvent}$ and I–$C_{solvent}$ atomic pairs, has a positive peak at approximately 4 Å and a negative peak at approximately 5.5 Å. The appearance of the positive peak at a shorter distance than the negative peak suggests that the average solute–solvent distance decreases due to the fragmen-

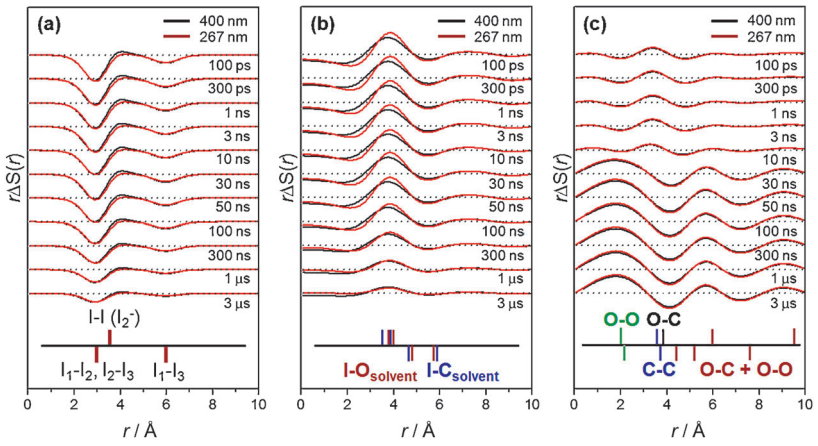

Figure 10. Difference RDFs, $r\Delta S(r)$, at various time delays were decomposed into three components: a) the solute-only term, b) the cage term, and c) the solvent-only term. The difference RDFs obtained with 400 nm excitation (black) and 267 nm excitation (red) are shown together. At the bottom of each plot, the distances of major atom–atom pairs are indicated as lines. The lines above the baseline correspond to the positive contributions reflecting the formation of reaction intermediates and products as well as the change in their associated solvent environment, whereas the lines below the baseline correspond to the negative contributions reflecting the depletion of the reactant (I_3^- ion) and the change in its related solvent environment.

tation of the I_3^- ion and formation of smaller cages. The wavelength dependence of the cage term is examined in Figure 11 b, in which the cage RDFs at 100 ps with 400 and 267 nm excitations are compared. As three-body dissociation generates more I atoms and I^- ions surrounded by methanol solvent than two-body dissociation, the number of cages with shorter solute–solvent distance increases with 267 nm excitation, which results in the larger amplitude of the positive peak at approximately 4 Å.

In Figure 11 c, the solvent RDFs at 100 ps with 400 and 267 nm excitations are shown. In general, the solvent term is dominated by the temperature increase before 10 ns and by the thermal expansion after 10 ns. The shapes of the solvent RDFs are the same for the two different excitation wavelengths, but the 267 nm RDF shows a slightly larger amplitude than the 400 nm RDF. This observation indicates that the temperature increase is larger with 267 nm excitation than with 400 nm excitation, as was discussed in the previous section.

3. Conclusions

We have investigated the structural dynamics of photodissociation of the I_3^- ion in methanol solution by using TRXL. From measurements at two different wavelengths (267 and 400 nm), we elucidated the change of reaction mechanism of I_3^- photolysis depending on the excitation wavelength. Upon 400 nm photoexcitation, the I_3^- ion undergoes only two-body dissociation into I_2^- and I. However, upon 267 nm photoexcitation, the I_3^- ion dissociates through both two-body dissociation ($I_2^- + I$) and three-body dissociation ($I^- + 2I$) with a 7:3 branching ratio. At both excitation wavelengths, the transient species recombine nongeminately to form the parent I_3^- ion in about 80 ns. Although previous spectroscopic studies suggested the possible involvement of the three-body dissociation pathway on excitation at 267 nm, we established the detailed reaction mechanism depending on the excitation wavelength by directly probing the structural changes of reacting molecules by using TRXL measurements. In addition, detailed structural dynamics for the solute/solvent cage and the changes in solvent density and temperature were revealed as a function of time. The results presented herein clearly demonstrate the power of TRXL for determining the structural dynamics of chemical reactions in the solution phase.

Experimental Section

Time-resolved X-ray liquidography (TRXL) makes use of an X-ray pulse, instead of an optical pulse, as a probe to generate a time-resolved X-ray scattering response that is sensitive to global molecular structure, as described in Figure 4. By analyzing the difference scattering patterns measured at various pump–probe time delays, the reaction dynamics can be revealed. For the data analysis, the maximum likelihood estimation (MLE) with the χ^2 estimator[13,14,18] was employed to globally fit the experimental curves by theoretically generated scattering curves. The theoretical scattering curves were calculated by using the standard diffuse X-ray scattering formula (Debye equation) based on the molecular structures optimized by a high-level DFT calculation and the pair distribution functions, $g(r)$, obtained from molecular dynamics (MD) simulation. More details of the TRXL method are given in the following sections and our previous studies.[12,17]

Experimental Setup for TRXL Data Collection

TRXL measurement was performed by using the laser pump–X-ray probe scheme at the beamline NW14A at KEK. Second and third harmonic generation of the output pulses from an amplified Ti:sapphire laser system provided femtosecond pulses at 400 and 267 nm center wavelengths at a repetition rate of 1 kHz. The laser pulses were stretched to approximately 2 ps by passing through fused silica rods to avoid multiphoton excitation of the sample. The laser beam was focused by a lens to a spot of 300 μm in diameter, where the laser beam overlapped with the X-ray beam with a crossing angle of 10°. At the sample, the pulse energy was approximately 40 to 60 μJ, which yielded a fluence of about 0.5 mJ mm^{-2}. The laser pulses were synchronized with X-ray pulses from the synchrotron by an active feedback control loop that adjusted the laser oscillator cavity length, and the relative time delay between the laser and X-ray pulses was controlled electronically. The time-delayed X-ray pulses were selected by using a synchronized mechanical chopper. A multilayer optic coated with depth-graded Ru/C layers (d = 40 Å, NTT Advanced Technology, Japan) produced a Gaussian-type X-ray spectrum with the center wavelength of 0.71 Å and approximately 5% energy bandwidth. The X-ray was used without being monochromatized. The blurring effect to the scattering curve due to the polychromaticity was not sub-

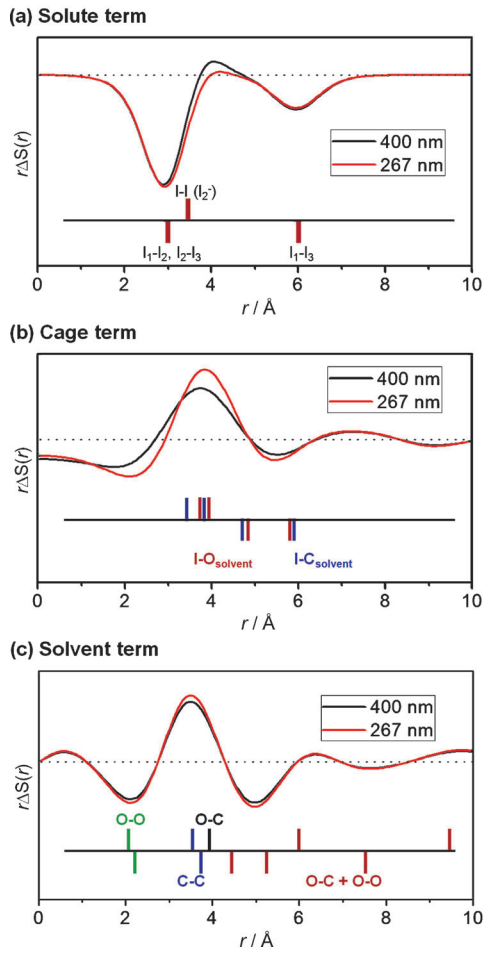

Figure 11. Decomposed difference RDFs, $r\Delta S(r)$, at 100 ps time delay. The difference RDFs with 400 nm excitation (black) and 267 nm excitation (red) are shown together. a) In the solute term, as the contribution of two-body dissociation (I_2^-) decreases with 267 nm excitation, the broad feature at 3–4 Å becomes less positive. b) In the cage term, since three-body dissociation generates more I atoms and I^- ions surrounded by methanol solvent than two-body dissociation, the number of cages with shorter solute–solvent distance increases with 267 nm excitation, thus resulting in the larger positive peak at approximately 4 Å. c) In the solvent term, the shapes of the RDFs are the same for the two different excitation wavelengths, but the 267 nm RDF has a slightly larger amplitude than the 400 nm RDF, thus indicating a larger temperature increase with 267 nm excitation than with 400 nm excitation.

stantial and was properly corrected by the polychromatic correction. The 100 ps long (full width at half maximum) X-ray pulses with 3×10^8 photons per pulse were focused into a $267\times290\ \mu m^2$ spot at the sample. The scattering patterns were collected with an area detector (MarCCD165, Mar USA) with a sample-to-detector distance of 40 mm. A 10 mM solution of I_3^- ions ($KI+I_2$ with 1:1 molar ratio) in methanol was circulated through the sapphire nozzle with 300 μm thick aperture and photoexcited by laser pulses. The laser-off images were acquired with the X-ray pulse arriving 3 ns earlier than the laser pulse (that is, time delay = −3 ns) to eliminate the contribution of the (unexcited) ground-state reactants. These laser-off images were used as a reference for calculating the time-resolved difference X-ray scattering patterns. A laser-off image was collected per three or four laser-on images to compensate for slow drifts of the X-ray intensity in the beamline. The scattering curves were measured at the following time delays:

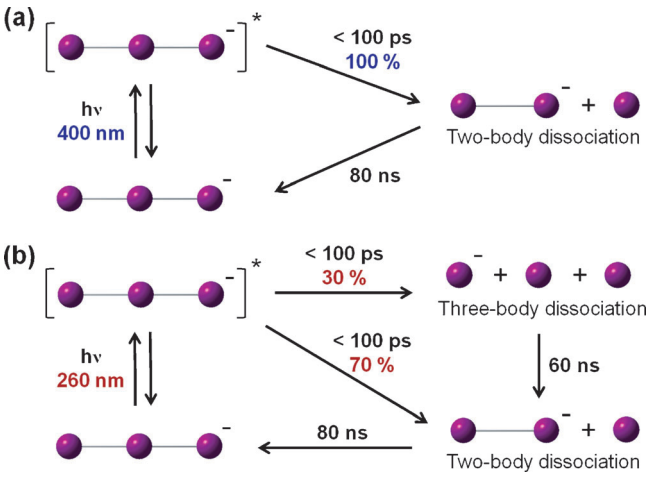

Figure 12. The reaction mechanisms of I_3^- photodissociation at a) 400 and b) 267 nm are summarized. The branching ratio and the timescale of each reaction step are indicated.

−3 ns, −100 ps, 100 ps, 300 ps, 1 ns, 3 ns, 10 ns, 30 ns, 50 ns, 100 ns, 300 ns, 1 μs, and 3 μs. To achieve a high signal-to-noise ratio, more than 50 images were acquired and averaged at each time delay.

Computational Details of DFT Calculations

All molecular structures were optimized by using the density functional theory (DFT) method.[46] Subsequent harmonic vibrational frequency calculations were performed on the optimized molecular structures. We used the recently developed ωB97X functional[47] as DFT exchange-correlation functional. It was found that ωB97X provides quite reasonable results for the molecular structures containing iodine atoms. To treat the scalar relativistic effect of iodine, we used the aug-cc-pVTZ-PP small-core relativistic effective core potential (RECP).[48] We also used the integral-equation-formalism polarizable continuum model (IEFPCM) method[49] to describe the solvent effect implicitly. All DFT calculations were performed by using the Gaussian 09 program.[50] Structural parameters are summarized in Table 1.

Data Analysis

Theoretical X-ray scattering intensities were calculated by using standard diffuse X-ray scattering formulas. The theoretical difference X-ray scattering curve, $\Delta S(q,t)_{theory}$, includes three components, that is, a solute-only term, a solute–solvent cross term, and a solvent-only term [Eq. (1)]:

$$\Delta S(q,t)_{\text{theory}} = \Delta S(q,t)_{\text{solute only}} + \Delta S(q,t)_{\text{solute-solvent}} + \Delta S(q,t)_{\text{solvent only}} = \left[\sum_k c_k(t)S_k - S_g(q)\sum_k c_k(0)\right] + (\partial S/\partial T)_\rho \Delta T(t) + (\partial S/\partial \rho)_T \Delta\rho(t) \quad (1)$$

in which k is the index of the solute species and $c_k(t)$ is the fractional concentration of each solute species as a function of time t. The solute-only term was calculated by the Debye equation using the molecular structures of solute species optimized by DFT calculation. We assumed that the scattering form factors of iodine atoms are all equal irrespective of the chemical species they belong to. The solute–solvent cross term was calculated by the

Debye equation using the pair distribution functions obtained from MD simulation. The solvent-only term was obtained by a separate solvent-heating experiment in which the pure solvent was vibrationally excited by near-infrared light.

Fitting and Error Analysis

To extract the structure of the I_3^- ion from the difference scattering intensity, the MLE with the χ^2 estimator[13,14,18] was employed with seven variable parameters. The variable parameters were five rate constants for all the reaction steps of photodissociation and recombination of the I_3^- ion (two-body dissociation, three-body dissociation, I_2 formation, recombination into I_2^- ion, and recombination into I_3^-), quantum yield, and scaling factor. The chi-squared (χ^2) value is given by Equation (2):

$$\chi^2(k_1,k_2,k_3,k_4,k_5,Q,A) = \frac{1}{N-p-1}\sum_i \frac{(\Delta S_{\text{theory}}(q_i) - \Delta S_{\text{expt}}(q_i))^2}{\sigma_i^2} \quad (2)$$

in which N is the total number of q points (=1080 for our experimental data), p is the number of fitting parameters (=7 without any constraint), and σ_i is the standard deviation at i^{th} q point. The likelihood (L) is related to χ^2 by Equation (3):

$$L(k_1,k_2,k_3,k_4,k_5,Q,A) \propto \exp(-\chi^2/2) \quad (3)$$

The errors of multiple fitting parameters are determined from this relationship by calculating the boundary values of 68.3% of the likelihood distribution. The calculation was performed by the MINUIT software package and the error values were provided by the MINOS algorithm in MINUIT. As we used the standard deviation of the measurement for calculation of χ^2, the quality of the fit became better as χ^2 approached 1.

Acknowledgements

This work was supported by the Institute for Basic Science (IBS), PRESTO/JST, the National Research Foundation of Korea (NRF) grant (No. 2007-0056095) funded by the Korean government (MSIP), and an Inha University Research Grant (INHA-48581). The work was carried out with the approval of the Photon Factory Program Advisory Committee (Proposal No. 2009S2-001 and 2010G553).

Keywords: iodine · photolysis · reaction mechanisms · structural dynamics · X-ray scattering

[1] A. H. Zewail, *Angew. Chem.* **2001**, *113*, 4501 – 4506; *Angew. Chem. Int. Ed.* **2001**, *40*, 4371 – 4375.
[2] M. Wall, A. N. Tarnovsky, T. Pascher, V. Sundstrom, E. Akesson, *J. Phys. Chem. A* **2003**, *107*, 211 – 217.
[3] X. M. Zheng, D. L. Phillips, *J. Phys. Chem. A* **2000**, *104*, 6880 – 6886.
[4] P. Kukura, D. W. McCamant, S. Yoon, D. B. Wandschneider, R. A. Mathies, *Science* **2005**, *310*, 1006 – 1009.
[5] H. Lee, Y. C. Cheng, G. R. Fleming, *Science* **2007**, *316*, 1462 – 1465.
[6] A. C. Moskun, A. E. Jailaubekov, S. E. Bradforth, G. H. Tao, R. M. Stratt, *Science* **2006**, *311*, 1907 – 1911.
[7] C. Bressler, C. Milne, V. T. Pham, A. El Nahhas, R. M. van der Veen, W. Gawelda, S. Johnson, P. Beaud, D. Grolimund, M. Kaiser, C. N. Borca, G. Ingold, R. Abela, M. Chergui, *Science* **2009**, *323*, 489 – 492.
[8] R. M. van der Veen, C. J. Milne, A. El Nahhas, F. A. Lima, V. T. Pham, J. Best, J. A. Weinstein, C. N. Borca, R. Abela, C. Bressler, M. Chergui, *Angew. Chem.* **2009**, *121*, 2749 – 2752; *Angew. Chem. Int. Ed.* **2009**, *48*, 2711 – 2714.
[9] H. D. Wen, N. Huse, R. W. Schoenlein, A. M. Lindenberg, *J. Chem. Phys.* **2009**, *131*, 234505.
[10] N. Huse, T. K. Kim, L. Jamula, J. K. McCusker, F. M. F. de Groot, R. W. Schoenlein, *J. Am. Chem. Soc.* **2010**, *132*, 6809 – 6816.
[11] J. Davidsson, J. Poulsen, M. Cammarata, P. Georgiou, R. Wouts, G. Katona, F. Jacobson, A. Plech, M. Wulff, G. Nyman, R. Neutze, *Phys. Rev. Lett.* **2005**, *94*, 245503.
[12] H. Ihee, M. Lorenc, T. K. Kim, Q. Y. Kong, M. Cammarata, J. H. Lee, S. Bratos, M. Wulff, *Science* **2005**, *309*, 1223 – 1227.
[13] M. Christensen, K. Haldrup, K. Bechgaard, R. Feidenhans'l, Q. Kong, M. Cammarata, M. Lo Russo, M. Wulff, N. Harrit, M. M. Nielsen, *J. Am. Chem. Soc.* **2009**, *131*, 502 – 508.
[14] K. Haldrup, M. Christensen, M. Cammarata, Q. Kong, M. Wulff, S. O. Mariager, K. Bechgaard, R. Feidenhans'l, N. Harrit, M. M. Nielsen, *Angew. Chem.* **2009**, *121*, 4244 – 4248; *Angew. Chem. Int. Ed.* **2009**, *48*, 4180 – 4184.
[15] K. Ichiyanagi, T. Sato, S. Nozawa, K. H. Kim, J. H. Lee, J. Choi, A. Tomita, H. Ichikawa, S. Adachi, H. Ihee, S. Koshihara, *J. Synchrotron Radiat.* **2009**, *16*, 391 – 394.
[16] H. Ihee, *Acc. Chem. Res.* **2009**, *42*, 356 – 366.
[17] T. K. Kim, J. H. Lee, M. Wulff, Q. Y. Kong, H. Ihee, *ChemPhysChem* **2009**, *10*, 1958 – 1980.
[18] S. Jun, J. H. Lee, J. Kim, K. H. Kim, Q. Kong, T. K. Kim, M. Lo Russo, M. Wulff, H. Ihee, *Phys. Chem. Chem. Phys.* **2010**, *12*, 11536 – 11547.
[19] Q. Kong, J. H. Lee, K. H. Kim, J. Kim, M. Wulff, H. Ihee, M. H. Koch, *J. Am. Chem. Soc.* **2010**, *132*, 2600 – 2607.
[20] M. Cammarata, M. Levantino, F. Schotte, P. A. Anfinrud, F. Ewald, J. Choi, A. Cupane, M. Wulff, H. Ihee, *Nat. Methods* **2008**, *5*, 881 – 886.
[21] H. S. Cho, N. Dashdorj, F. Schotte, T. Graber, R. Henning, P. Anfinrud, *Proc. Natl. Acad. Sci. USA* **2010**, *107*, 7281 – 7286.
[22] J. Kim, K. H. Kim, J. G. Kim, T. W. Kim, Y. Kim, H. Ihee, *J. Phys. Chem. Lett.* **2011**, *2*, 350 – 356.
[23] A. Plech, V. Kotaidis, M. Lorenc, J. Boneberg, *Nat. Phys.* **2006**, *2*, 44 – 47.
[24] A. Plech, V. Kotaidis, K. Istomin, M. Wulff, *J. Synchrotron Radiat.* **2007**, *14*, 288 – 294.
[25] A. Plech, V. Kotaidis, A. Siems, M. Sztucki, *Phys. Chem. Chem. Phys.* **2008**, *10*, 3888 – 3894.
[26] S. Ibrahimkutty, J. Kim, M. Cammarata, F. Ewald, J. Choi, H. Ihee, A. Plech, *ACS Nano* **2011**, *5*, 3788 – 3794.
[27] U. Banin, S. Ruhman, *J. Chem. Phys.* **1993**, *98*, 4391 – 4403.
[28] U. Banin, A. Waldman, S. Ruhman, *J. Chem. Phys.* **1992**, *96*, 2416 – 2419.
[29] T. Kühne, R. Kuster, P. Vohringer, *Chem. Phys.* **1998**, *233*, 161 – 178.
[30] T. Kühne, P. Vohringer, *J. Chem. Phys.* **1996**, *105*, 10788 – 10802.
[31] T. Kühne, P. Vohringer, *J. Phys. Chem. A* **1998**, *102*, 4177 – 4185.
[32] L. Zhu, K. Takahashi, M. Saeki, T. Tsukuda, T. Nagata, *Chem. Phys. Lett.* **2001**, *350*, 233 – 239.
[33] H. Sato, F. Hirata, A. B. Myers, *J. Phys. Chem. A* **1998**, *102*, 2065 – 2071.
[34] C. J. Margulis, D. F. Coker, R. M. Lynden-Bell, *Chem. Phys. Lett.* **2001**, *341*, 557 – 560.
[35] C. J. Margulis, D. F. Coker, R. M. Lynden-Bell, *J. Chem. Phys.* **2001**, *114*, 367 – 376.
[36] F. S. Zhang, R. M. Lynden-Bell, *Phys. Rev. Lett.* **2003**, *90*, 185505.
[37] A. E. Johnson, A. B. Myers, *J. Phys. Chem.* **1996**, *100*, 7778 – 7788.
[38] E. Gershgoren, U. Banin, S. Ruhman, *J. Phys. Chem. A* **1998**, *102*, 9 – 16.
[39] M. Cammarata, M. Lorenc, T. K. Kim, J. H. Lee, Q. Y. Kong, E. Pontecorvo, M. Lo Russo, G. Schiro, A. Cupane, M. Wulff, H. Ihee, *J. Chem. Phys.* **2006**, *124*, 124504.
[40] T. K. Kim, M. Lorenc, J. H. Lee, M. Russo, J. Kim, M. Cammarata, Q. Y. Kong, S. Noel, A. Plech, M. Wulff, H. Ihee, *Proc. Natl. Acad. Sci. USA* **2006**, *103*, 9410 – 9415.
[41] Q. Y. Kong, J. H. Lee, A. Plech, M. Wulff, H. Ihee, M. H. J. Koch, *Angew. Chem.* **2008**, *120*, 5632 – 5635; *Angew. Chem. Int. Ed.* **2008**, *47*, 5550 – 5553.
[42] J. H. Lee, J. Kim, M. Cammarata, Q. Kong, K. H. Kim, J. Choi, T. K. Kim, M. Wulff, H. Ihee, *Angew. Chem.* **2008**, *120*, 1063 – 1066; *Angew. Chem. Int. Ed.* **2008**, *47*, 1047 – 1050.

[43] K. H. Kim, S. Muniyappan, K. Y. Oang, J. G. Kim, S. Nozawa, T. Sato, S. Y. Koshihara, R. Henning, I. Kosheleva, H. Ki, Y. Kim, T. W. Kim, J. Kim, S. Adachi, H. Ihee, *J. Am. Chem. Soc.* **2012**, *134*, 7001 – 7008.
[44] K. H. Kim, J. H. Lee, J. Kim, S. Nozawa, T. Sato, A. Tomita, K. Ichiyanagi, H. Ki, J. Kim, S. Adachi, H. Ihee, *Phys. Rev. Lett.* **2013**, *110*, 165505.
[45] J. H. Lee, M. Wulff, S. Bratos, J. Petersen, L. Guerin, J. C. Leicknam, M. Carnmarata, Q. Kong, J. Kim, K. B. Moller, H. Ihee, *J. Am. Chem. Soc.* **2013**, *135*, 3255 – 3261.
[46] J. Kim, T. K. Kim, H. Ihee, *J. Phys. Chem. A* **2011**, *115*, 1264 – 1271.
[47] J.-D. Chai, M. Head-Gordon, *Phys. Chem. Chem. Phys.* **2008**, *10*, 6615 – 6620.
[48] K. A. Peterson, B. C. Shepler, D. Figgen, H. Stoll, *J. Phys. Chem. A* **2006**, *110*, 13877 – 13883.
[49] E. Cancès, B. Mennucci, J. Tomasi, *J. Chem. Phys.* **1997**, *107*, 3032 – 3041.
[50] Gaussian 09 (Revision D.01), M. J. Frisch, G. W. Trucks, H. B. Schlegel, G. E. Scuseria, M. A. Robb, J. R. Cheeseman, G. Scalmani, V. Barone, B. Mennucci, G. A. Petersson, H. Nakatsuji, M. Caricato, X. Li, H. P. Hratchian, A. F. Izmaylov, J. Bloino, G. Zheng, J. L. Sonnenberg, M. Hada, M. Ehara, K. Toyota, R. Fukuda, J. Hasegawa, M. Ishida, T. Nakajima, Y. Honda, O. Kitao, H. Nakai, T. Vreven, J. A. Montgomery, Jr., J. E. Peralta, F. Ogliaro, M. Bearpark, J. J. Heyd, E. Brothers, K. N. Kudin, V. N. Staroverov, R. Kobayashi, J. Normand, K. Raghavachari, A. Rendell, J. C. Burant, S. S. Iyengar, J. Tomasi, M. Cossi, N. Rega, J. M. Millam, M. Klene, J. E. Knox, J. B. Cross, V. Bakken, C. Adamo, J. Jaramillo, R. Gomperts, R. E. Stratmann, O. Yazyev, A. J. Austin, R. Cammi, C. Pomelli, J. W. Ochterski, R. L. Martin, K. Morokuma, V. G. Zakrzewski, G. A. Voth, P. Salvador, J. J. Dannenberg, S. Dapprich, A. D. Daniels, Ö. Farkas, J. B. Foresman, J. V. Ortiz, J. Cioslowski, D. J. Fox, Gaussian, Inc., Wallingford, CT, **2009**.

Received: August 2, 2013
Published online on October 2, 2013